

---

# TT-FSI: Scalable Faithful Shapley Interactions via Tensor-Train

---

Ungsik Kim  
 Gyeongsang National University  
 b1peng@gnu.ac.kr

Suwon Lee\*  
 Gyeongsang National University  
 leesuwon@gnu.ac.kr

## Abstract

The Faithful Shapley Interaction (FSI) index uniquely satisfies the faithfulness axiom among Shapley interaction indices, but computing FSI requires  $O(d^\ell \cdot 2^d)$  time and existing implementations use  $O(4^d)$  memory. We present **TT-FSI**, which exploits FSI’s algebraic structure via Matrix Product Operators (MPO). Our main theoretical contribution is proving that the linear operator  $v \mapsto \text{FSI}(v)$  admits an MPO representation with TT-rank  $O(\ell d)$ , enabling an efficient sweep algorithm with  $O(\ell^2 d^3 \cdot 2^d)$  time and  $O(\ell d^2)$  core storage—an exponential improvement over existing methods. Experiments on six datasets ( $d = 8$  to  $d = 20$ ) demonstrate up to  $280\times$  speedup over baseline,  $85\times$  over SHAP-IQ, and  $290\times$  memory reduction. TT-FSI scales to  $d = 20$  (1M coalitions) where all competing methods fail.

## 1 Introduction

Shapley values have become the de facto standard for feature attribution in explainable AI [5], yet they are fundamentally limited to *additive* explanations: each feature receives an independent contribution score, and these scores sum to the model output. This additive structure cannot capture *interaction effects*—cases where features jointly contribute more (or less) than the sum of their individual effects. In tree ensembles and neural networks, such interactions often encode the most decision-relevant patterns, yet they remain invisible to standard SHAP analysis.

Shapley interaction indices address this gap by quantifying joint contributions of feature subsets [31, 16, 15]. Among proposed indices, the **Faithful Shapley Interaction (FSI)** [42] is uniquely characterized by the *faithfulness axiom*: FSI scores induce the optimal  $\ell$ -order surrogate that minimizes Shapley-weighted approximation error. This optimality guarantee is absent in alternatives such as STII [40] and SII [16], making FSI the principled choice when explanation fidelity matters.

Despite its theoretical appeal, computing FSI is computationally challenging. The closed-form solution involves evaluating all  $2^d$  coalitions and performing operations that scale as  $O(d^\ell \cdot 2^d)$  for fixed interaction order  $\ell$ , or  $O(3^d)$  when  $\ell = d$ . For moderate-dimensional data ( $d \geq 15$ ), this becomes prohibitively expensive. Existing implementations such as SHAP-IQ [28] in exact mode call `np.diag()` on a  $2^d$ -length vector, materializing a dense  $2^d \times 2^d$  matrix and causing  $O(4^d)$  memory consumption.

**Our Approach.** Recent work IT-SHAP [19] demonstrated that the Shapley-Taylor Interaction Index (STII) admits efficient computation via Tensor-Train (TT) decomposition, exploiting STII’s discrete derivative structure. However, FSI—defined as the solution to a weighted least squares optimization problem (Eq. 2)—appears structurally incompatible with such methods. While STII admits local prefix-based transitions yielding TT-rank  $O(d)$ , FSI seems to require global regression over all coalitions.

---

\*(Corresponding author)

Our key insight is that FSI’s closed-form solution (Theorem 19 of [42]) can be decomposed into two operations—a Möbius transform and a correction term—both of which admit efficient TT representations. The Möbius transform has Kronecker product structure, giving it TT-rank 1. The correction term, despite its complex combinatorial weighting, depends only on subset *cardinalities*  $|S|$  and  $|T|$ , not on which specific features are included. This cardinality-dependence means we can compute it using an operator that tracks only two counters, yielding TT-rank  $O(\ell d)$ .

**Contributions.** We present **TT-FSI**, a novel algorithm exploiting this algebraic structure. Our contributions build upon each other:

1. **Theoretical foundation:** We prove that the linear operator  $v \mapsto \text{FSI}(v)$  admits a Matrix Product Operator (MPO) representation with TT-rank  $O(\ell d)$ . This result—exploiting the TT structure of the *operator itself*, not of the input  $v$ —enables the following algorithmic contribution.
2. **Efficient algorithm:** Building on the MPO representation, we develop a left-to-right sweep algorithm achieving time complexity  $O(\ell^2 d^3 \cdot 2^d)$  and core storage  $O(\ell d^2)$ —an exponential memory improvement over existing  $O(4^d)$  methods.
3. **Empirical validation:** We demonstrate that this theoretical and algorithmic framework translates to practical gains: up to  $280\times$  speedup over baseline,  $85\times$  over SHAP-IQ, and  $290\times$  memory reduction on six real-world datasets ( $d = 8$  to  $d = 20$ ). TT-FSI computes FSI for  $d = 20$  (over 1 million coalitions) in under 10 seconds, where all competing methods fail.

## 2 Background

This section introduces the key concepts needed to understand TT-FSI. We first review Shapley values (§2.1), then discuss interaction indices with focus on FSI (§2.2), and finally introduce the Tensor-Train decomposition that enables our efficient algorithm (§2.3).

### 2.1 Cooperative Game Theory and Shapley Values

Let  $[d] = \{1, 2, \dots, d\}$  be a set of  $d$  players (features). A *cooperative game* is defined by a value function  $v : 2^{[d]} \rightarrow \mathbb{R}$  that assigns a worth to each coalition  $S \subseteq [d]$ , with  $v(\emptyset) = 0$ . In the context of machine learning,  $v(S)$  typically represents the model’s prediction when only features in  $S$  are present (with features in  $[d] \setminus S$  marginalized out).

The **Shapley value** [36] assigns to each player  $i$  a fair share of the total worth:

$$\phi_i(v) = \sum_{S \subseteq [d] \setminus \{i\}} \frac{|S|!(d - |S| - 1)!}{d!} [v(S \cup \{i\}) - v(S)]. \quad (1)$$

The Shapley value satisfies several desirable axioms including efficiency ( $\sum_i \phi_i = v([d]) - v(\emptyset)$ ), symmetry, linearity, and null player properties.

### 2.2 Shapley Interaction Indices

Various interaction indices extend Shapley values to feature subsets, including SII [16], k-SII, STII [40], and BII (see Appendix A for definitions). Among these, the **Faithful Shapley Interaction (FSI)** [42] is uniquely characterized by the *faithfulness axiom*: the interaction scores induce the optimal  $\ell$ -order polynomial surrogate under Shapley-weighted regression. FSI is defined as:

$$\min_{\{I_S\}_{|S| \leq \ell}} \sum_{T \subseteq [d]} w_T \left( v(T) - \sum_{S \subseteq T, |S| \leq \ell} I_S \right)^2, \quad (2)$$

with specific weights  $w_T$  derived from Shapley’s axioms. The resulting surrogate  $g(T) = \sum_{S \subseteq T, |S| \leq \ell} I_S$  is the unique *faithful* approximation: for  $\ell$ -additive games (where  $v$  has Möbius support on  $|S| \leq \ell$ ), FSI recovers  $v$  exactly.

**Closed-Form Solution.** While the optimization problem (2) appears to require solving a weighted least squares system over  $2^d$  coalitions, the special structure of Shapley weights admits a remarkably compact solution. Tsai et al. [42] proved that FSI has a closed-form (their Theorem 19):

$$E_S^{\text{FSI}}(v, \ell) = a(v, S) + C_S(v, \ell), \quad (3)$$

where  $a(v, S) = \sum_{T \subseteq S} (-1)^{|S|-|T|} v(T)$  is the **Möbius transform** and  $C_S(v, \ell)$  is a **correction term**:

$$C_S(v, \ell) = (-1)^{\ell-|S|} \frac{|S|}{\ell+|S|} \binom{\ell}{|S|} \sum_{\substack{T \supseteq S \\ |T| > \ell}} \frac{\binom{|T|-1}{\ell}}{\binom{|T|+\ell-1}{\ell+|S|}} a(v, T). \quad (4)$$

This correction term adjusts the Möbius transform to ensure faithfulness, and it only involves coalitions  $T$  with  $|T| > \ell$ .

### 2.3 Tensor-Train Decomposition

The **Tensor-Train (TT) decomposition** [30, 23] represents a  $d$ -dimensional tensor  $\mathcal{A} \in \mathbb{R}^{n_1 \times \dots \times n_d}$  as a product of 3-way tensors (cores):

$$\mathcal{A}_{i_1, \dots, i_d} = \sum_{\alpha_1, \dots, \alpha_{d-1}} G_{i_1, \alpha_1}^{(1)} G_{\alpha_1, i_2, \alpha_2}^{(2)} \cdots G_{\alpha_{d-1}, i_d}^{(d)}. \quad (5)$$

The **TT-rank** is the tuple  $(r_1, \dots, r_{d-1})$  where  $r_k$  is the dimension of the bond index  $\alpha_k$ . A key property is that tensors with low TT-rank can be stored and manipulated efficiently in  $O(dnr^2)$  space and time, where  $r = \max_k r_k$  and  $n = \max_k n_k$ .

**Matrix Product Operators (MPO).** For our purposes, we work with *Matrix Product Operators* [35], which represent linear maps  $M : \mathbb{R}^{2^d} \rightarrow \mathbb{R}^{2^d}$  in TT format:

$$M_{\sigma, \tau} = \sum_{\alpha_1, \dots, \alpha_{d-1}} G_{\sigma_1, \tau_1, \alpha_1}^{(1)} G_{\alpha_1, \sigma_2, \tau_2, \alpha_2}^{(2)} \cdots G_{\alpha_{d-1}, \sigma_d, \tau_d}^{(d)}, \quad (6)$$

where  $\sigma = (\sigma_1, \dots, \sigma_d)$  and  $\tau = (\tau_1, \dots, \tau_d)$  are binary indices representing subsets.

**Why TT Matters for FSI.** A central advantage of TT decomposition is that *operators with specific algebraic structures often admit low TT-rank representations*. If an operator  $M$  can be written as a Kronecker product  $M = \bigotimes_{i=1}^d M_i$  of small matrices, it has TT-rank 1 (Lemma 2 in Appendix C). More generally, operators that “locally” process each dimension with bounded state tracking can be represented with polynomial TT-rank.

The Möbius operator  $\mu_{\downarrow}$  on the Boolean lattice—central to FSI computation—has precisely such a Kronecker structure:  $\mu_{\downarrow} = \bigotimes_{i=1}^d M_i$  where  $M_i = \begin{pmatrix} 1 & 0 \\ -1 & 1 \end{pmatrix}$ . This implies  $\mu_{\downarrow}$  has **TT-rank 1** and can be applied in  $O(d \cdot 2^d)$  time (see Appendix B).

Recent work IT-SHAP [19] exploited this structure for the Shapley-Taylor Interaction Index (STII), which has a single-counter structure yielding TT-rank  $O(d)$ . However, FSI’s correction term (Eq. 4) requires tracking *two* counters— $|S|$  and  $|T|$ —increasing TT-rank to  $O(\ell d)$ . Despite this added complexity, the cardinality-dependence still enables polynomial-rank representation, as we formalize in §4.

## 3 Related Work

Before presenting our algorithm, we situate TT-FSI within the context of landscape of explainability methods and tensor decomposition techniques.

**Shapley-based Explanations.** LIME [33] pioneered local surrogate-based explanations, while earlier work by Štrumbelj and Kononenko [39] developed Shapley-based feature contributions.

SHAP [26] unified several feature attribution methods under the Shapley value framework, becoming central to modern XAI [17]. Covert et al. [11] provide a comprehensive taxonomy of removal-based explanations unifying 26 methods. Integrated Gradients [41] provides an axiomatic approach for neural networks. TreeSHAP [25] enables polynomial-time exact computation for tree models by exploiting tree structure. FastSHAP [22] trains an auxiliary model to predict Shapley values in real-time, trading exactness for speed.

**Interaction Indices.** Beyond Shapley-based methods, statistical approaches such as the H-statistic [14] and functional ANOVA decomposition [20] measure feature interactions through variance partitioning. In game-theoretic approaches, the Shapley Interaction Index (SII) [16] and Shapley-Taylor Interaction Index (STII) [40] extend Shapley values to interactions but lack faithfulness. Faith-Shap (FSI) [42] is the unique faithful interaction index.

**Efficient Computation.** Computing Shapley values is #P-hard in general [43, 3], motivating both exact algorithms for tractable model classes and sampling-based approximations. The choice between interventional and observational conditionals [21] and between model-faithful and data-faithful explanations [9] further complicates evaluation, while adversarial vulnerabilities of post-hoc methods [37] underscore the need for principled approaches. The shapiq library [28, 28] provides a unified framework for computing various interaction indices, including both exact and approximate methods. Its exact mode (SHAP-IQ) scales poorly with dimension, creating dense  $2^d \times 2^d$  matrices via `np.diag()` and causing  $O(4^d)$  memory consumption. Sampling-based alternatives [8, 27] such as SVARM-IQ [24] use stratified sampling to estimate interaction indices with probabilistic guarantees, achieving polynomial sample complexity for fixed approximation error. Extensions handle dependent features [1] and global importance aggregation [12]. These sampling approaches excel when approximate values suffice, but exact computation remains necessary for rigorous analysis, debugging model behavior, and benchmarking approximation methods—precisely the use cases TT-FSI addresses.

**Tensor Networks.** Tensor-Train decomposition [30, 10] and Matrix Product States [35] originated in numerical linear algebra and quantum physics. Connections between tensor networks and graphical models [34] provide additional theoretical grounding. Recent work has applied tensor networks to machine learning [38, 29]. TT-FSI makes no assumption on  $v$ ; we exploit the TT structure of the *FSI operator* rather than the input.

**Relation to IT-SHAP.** IT-SHAP [19] applied TT decomposition to the Shapley-Taylor Interaction Index (STII), achieving substantial speedups. STII’s success stems from its combinatorial simplicity: discrete derivatives yield weights depending on a *single* cardinality, representable by a single-counter finite state machine with TT-rank  $O(d)$ . FSI, by contrast, is defined implicitly via weighted least squares (Eq. 2)—an optimization problem rather than a direct formula—making it appear structurally incompatible with tensor methods. Indeed, IT-SHAP does not mention FSI, leaving the “least squares class” of interaction indices outside tensor-based approaches.

We show that this incompatibility is only superficial. By analyzing Tsai et al.’s closed-form solution [42], we discover that FSI decomposes into incidence algebra operations: a rank-1 Möbius transform plus a correction term whose weights depend on *two* cardinalities ( $|S|$  and  $|T|$ ). This two-counter structure admits a finite state machine with  $O(\ell d)$  states—still tractable. TT-FSI thus extends tensor methods beyond combinatorially-defined indices to the optimization-defined FSI, bridging a gap that prior work left unaddressed.

## 4 Method: TT-FSI

### 4.1 Overview

FSI’s closed-form (Eq. 3) naturally decomposes into two operations: the **Möbius transform**  $a(v, S)$ , which extracts the “pure” interaction contribution of subset  $S$  by removing redundant contributions from smaller coalitions, and a **correction term**  $C_S(v, \ell)$ , which redistributes contributions from large coalitions ( $|T| > \ell$ ) to ensure faithfulness.

Both operations are *linear* in  $v$ . The Möbius transform  $a(v, S) = \sum_{T \subseteq S} (-1)^{|S|-|T|} v(T)$  is a linear combination of value function entries, computed by the operator  $\mu_\downarrow$ . The correction term (Eq. 4) sums over  $a(v, T)$  for  $|T| > \ell$ —itself linear in  $v$ —with coefficients depending only on cardinalities  $|S|$  and  $|T|$ , computed by the operator  $A_{\text{trunc}}$ . We thus view FSI as a linear operator mapping  $v \in \mathbb{R}^{2^d}$  to interaction scores:

$$E^{\text{FSI}}(v, \ell) = \underbrace{\mu_\downarrow \cdot v}_{\text{Möbius transform}} + \underbrace{A_{\text{trunc}} \cdot (\mu_\downarrow \cdot v)}_{\text{Correction term}}, \quad (7)$$

where  $\mu_\downarrow$  is the Möbius operator and  $A_{\text{trunc}}$  is a correction MPO. Our key insight is that *both operations admit efficient TT representations*: the Möbius transform has TT-rank 1 due to its Kronecker structure (§4.2), and the correction term has TT-rank  $O(\ell d)$  because it only needs to track two bounded counters (§4.3).

**Roadmap.** We proceed as follows: (a) establish the TT structure of each component—Möbius transform (§4.2) and correction term (§4.3); (b) develop an efficient sweep algorithm to apply the combined MPO (§4.4); (c) introduce a precontraction optimization (§4.5); and (d) analyze the resulting complexity (§4.6).

## 4.2 Möbius Transform as Rank-1 MPO

The Möbius transform  $a(v, S) = \sum_{T \subseteq S} (-1)^{|S|-|T|} v(T)$  can be computed by applying the operator  $\mu_\downarrow$  to the value function vector  $v$ . Due to the Kronecker structure, each core is:

$$G_{\text{Möb}}^{(k)}[\sigma_k, \tau_k] = M[\sigma_k, \tau_k] = \begin{cases} 1 & \sigma_k = 0, \tau_k = 0 \\ 1 & \sigma_k = 1, \tau_k = 1 \\ -1 & \sigma_k = 1, \tau_k = 0 \\ 0 & \text{otherwise} \end{cases} \quad (8)$$

Since all cores have bond dimension 1, the Möbius transform has **TT-rank 1** and can be computed in  $O(d \cdot 2^d)$  time.

## 4.3 Correction Term as Polynomial-Rank MPO

The correction term in Equation (4) involves summing over supersets  $T \supset S$  with  $|T| > \ell$ , weighting by coefficients that depend on  $|S|$  and  $|T|$ , and filtering to outputs with  $|S| \leq \ell$ .

**Intuition: Why Polynomial Rank?** The correction term can be computed by an operator that processes each feature dimension sequentially, tracking only *two counters*: the running size of the output set  $|S|$  and the running size of the input set  $|T|$ . Since the weights depend only on these cardinalities (not on which specific features are included), we can model this computation as a *finite-state machine* with state space  $(|S|, |T|)$ . At each position  $k$ , the number of possible states is bounded by  $O(\ell k)$  because  $|S| \leq \ell$ . This finite-state structure naturally maps to an MPO with polynomial TT-rank—far smaller than the exponential  $2^d$  that would be required by a naive approach. Figure 1 illustrates this structure for  $d = 3$  and  $\ell = 2$ .

We now formalize this intuition. The key insight is that the abstract state  $(|S|, |T|)$  can be tracked incrementally: at each position  $k$ , we maintain *running counts*  $(s_k, t_k)$  representing the partial sums accumulated so far, which equal  $(|S|, |T|)$  at the final position  $k = d$ .

**Formal Construction.** We construct an MPO  $A_{\text{trunc}}$  that realizes the finite-state machine described above. The MPO’s bond indices encode the running state  $(s_k, t_k)$ , where  $s_k = \sum_{i=1}^k \sigma_i$  is the running count of output bits (size of  $S$ ) and  $t_k = \sum_{i=1}^k \tau_i$  is the running count of input bits (size of  $T$ ).

**State Space.** At position  $k$ , the state space is:

$$\{(s, t) : 0 \leq s \leq \min(k, \ell), 0 \leq t \leq k, t \geq s\} \quad (9)$$

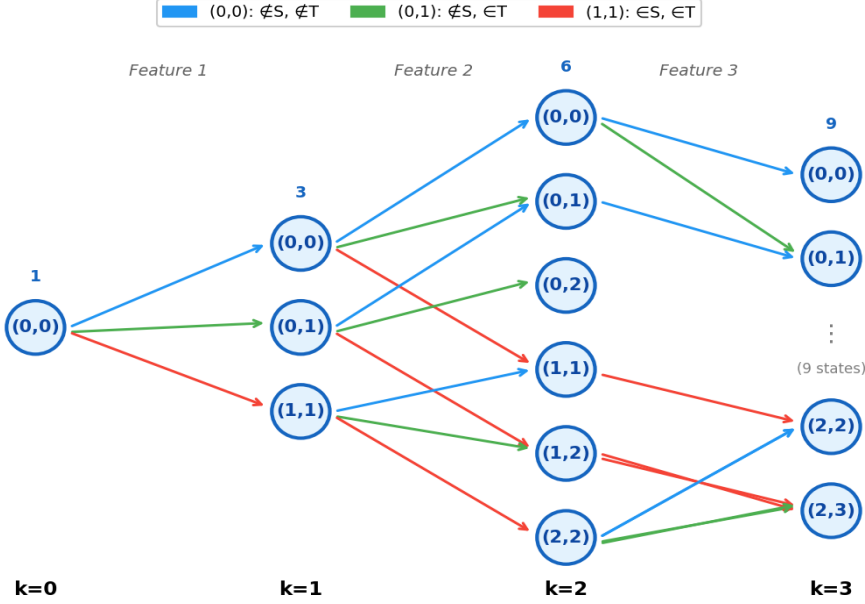


Figure 1: Finite-state machine for correction operator ( $d = 3, \ell = 2$ ). States  $(s, t)$  track cumulative counts. Colors: blue ( $\notin S, \notin T$ ), green ( $\notin S, \in T$ ), red ( $\in S \cap T$ ). State count grows polynomially:  $1 \rightarrow 3 \rightarrow 6 \rightarrow 9$ .

The constraint  $s \leq \min(k, \ell)$  implements the truncation to interaction order  $\ell$ . The constraint  $t \geq s$  is a *derived necessary condition*: we enforce the per-bit constraint  $\tau_i \geq \sigma_i$  in local transitions (see below), which implies  $t_k \geq s_k$  automatically. The state constraint helps bound the number of reachable states.

**Bond Dimension.** Note that while the constraint  $t \geq s$  reduces the exact count of valid states, the number of states is *upper bounded by*:

$$D_k \leq (\min(k, \ell) + 1)(k + 1) = O(\ell k), \quad (10)$$

which suffices for our TT-rank analysis. The maximum bond dimension is thus  $D_{\max} = O(\ell d)$ .

**Lemma 1** (TT-rank upper bound). *The TT-rank of  $A_{\text{trunc}}$  at bond  $k$  is upper bounded by the number of reachable states, i.e.,  $O(\ell k)$ . The maximum TT-rank is thus  $O(\ell d)$ . (Proof in Appendix C.)*

**Core Construction.** For internal sites  $k = 1, \dots, d-1$ , the core implements pure state transitions:

$$G^{(k)}[\alpha_{\text{prev}}, \sigma, \tau, \alpha_{\text{next}}] = \begin{cases} 1 & \text{if valid transition} \\ 0 & \text{otherwise} \end{cases} \quad (11)$$

A transition is valid if: (i)  $\tau \geq \sigma$  (per-bit superset enforcement: if  $\sigma_k = 1$  then  $\tau_k = 1$ ); (ii)  $s_{\text{next}} = s_{\text{prev}} + \sigma$  and  $t_{\text{next}} = t_{\text{prev}} + \tau$  (counter updates); and (iii)  $s_{\text{next}} \leq \min(k, \ell)$  (output truncation).

For the final site  $k = d$ , the core applies the weight function:

$$G^{(d)}[\alpha_{\text{prev}}, \sigma, \tau, 0] = \begin{cases} w(s, t) & \text{if valid and } s \leq \ell, t > \ell \\ 0 & \text{otherwise} \end{cases} \quad (12)$$

where the weight  $w(s, t)$  extracts the coefficient from the correction formula (Eq. 4), substituting  $s = |S|$  and  $t = |T|$  (correctness proof in Lemma 4):

$$w(s, t) = (-1)^{\ell-s} \cdot \frac{s}{\ell+s} \cdot \binom{\ell}{s} \cdot \frac{\binom{t-1}{\ell}}{\binom{t+\ell-1}{\ell+s}}. \quad (13)$$

---

**Algorithm 1** Efficient MPO-Vector Contraction (Left-to-Right Sweep)

---

**Require:** MPO cores  $\{G^{(k)}\}_{k=1}^d$ , input vector  $v \in \mathbb{R}^{2^d}$   
**Ensure:** Output vector  $u = M \cdot v$

- 1:  $X \leftarrow v$  reshaped to  $(1, 1, 2^d)$  {(out-prefix, bond, in-suffix)}
- 2: **for**  $k = 1$  to  $d$  **do**
- 3:    $\{X \in \mathbb{R}^{2^{k-1} \times D_{k-1} \times 2^{d-k+1}}\}$
- 4:   Reshape  $X$  to  $(2^{k-1} \cdot D_{k-1}, 2, 2^{d-k})$  {merge, split off  $\tau_k$ }
- 5:   Contract:  $X'[m, \sigma, \beta, r] \leftarrow \sum_{\tau, \alpha} X[m', \tau, r] \cdot G^{(k)}[\alpha, \sigma, \tau, \beta]$
- 6:   Reshape  $X'$  to  $(2^k, D_k, 2^{d-k})$  {expand out-prefix with  $\sigma_k$ }
- 7:    $X \leftarrow X'$
- 8: **end for**
- 9: Reshape  $X$  to  $u \in \mathbb{R}^{2^d}$
- 10: **return**  $u$

---

**Numerical Stability.** To avoid overflow in binomial coefficients for large  $d$ , we compute weights using log-gamma functions. The complete log-stable implementation is provided in Algorithm 2 of the Supplementary Material.

The preceding construction yields an MPO with polynomial TT-rank  $O(\ell d)$ , but naive application to a value function vector would still require exponential time. The next section addresses this computational challenge.

#### 4.4 Efficient MPO Contraction

The polynomial TT-rank  $O(\ell d)$  established in §4.3 is the key enabler of efficient computation. A naive implementation of MPO-vector multiplication iterates over all  $2^d \times 2^d$  input-output pairs, resulting in  $O(4^d \cdot D)$  complexity—worse than brute-force FSI. However, the TT structure allows us to avoid this exponential blowup: we employ a **left-to-right sweep** that processes one dimension at a time, maintaining an intermediate tensor that contracts the MPO core with the input progressively. Algorithm 1 formalizes this approach.

**Intermediate Tensor Structure.** At each step  $k$ , the intermediate tensor has shape  $(2^{k-1}, D_{k-1}, 2^{d-k+1})$ , where the three dimensions represent partial output configurations  $(\sigma_1, \dots, \sigma_{k-1})$ , MPO bond states encoding  $(s_{k-1}, t_{k-1})$  counters, and remaining input configurations  $(\tau_k, \dots, \tau_d)$ , respectively.

**Remark.** While the output dimension appears as  $2^d$ , the correction MPO produces non-zero outputs *only* for  $|S| \leq \ell$  due to the truncation constraint in the state space. The  $O(2^d)$  intermediate size is unavoidable because we must read the full input  $v \in \mathbb{R}^{2^d}$ . Optionally, one can compress the output-prefix dimension by storing only prefixes with  $s_k \leq \ell$ , reducing  $2^k$  to  $\sum_{s \leq \ell} \binom{k}{s}$ ; we use the dense representation for simplicity since input I/O dominates memory.

**Sparse Core Storage.** The MPO cores are highly sparse. For each input state  $\alpha_{\text{prev}}$ , there are at most 3 valid transitions corresponding to  $(\sigma, \tau) \in \{(0, 0), (0, 1), (1, 1)\}$  (since  $\tau \geq \sigma$ ). Thus each core  $G^{(k)}$  has  $O(D_{k-1})$  nonzero entries, and total storage is  $O(\ell d^2)$  (Lemma 7), which is even tighter than the dense bound  $O(\ell^2 d^3)$ .

Each contraction step costs  $O(2^k \cdot D_{k-1} \cdot D_k \cdot 2^{d-k})$ . Summing over all  $k$  yields  $O(\ell^2 d^3 \cdot 2^d)$  (detailed derivation in Lemma 5). This bound is conservative. Since transitions are *deterministic* (each  $(\alpha_{\text{prev}}, \sigma, \tau)$  maps to at most one  $\alpha_{\text{next}}$ ), exploiting sparsity can reduce the per-step cost to depend on  $\text{nnz}(G^{(k)}) = O(D_{k-1})$  rather than  $D_{k-1} \cdot D_k$ , explaining why empirical runtimes often beat the theoretical upper bound.

Table 1: Complexity comparison of FSI computation methods. “Core Space” denotes storage for algorithm-specific data structures, excluding the  $O(2^d)$  input/output vectors common to all methods.

Method	Time	Core Space	Space Complexity
Baseline [42]	$O(d^\ell \cdot 2^d)$	$O(1)$	$O(2^d)$
SHAP-IQ [28]	$O(d^{2\ell} \cdot 2^d)$	$O(4^d)$	$O(4^d)$
TT-FSI (ours)	$O(\ell^2 d^3 \cdot 2^d)$	$O(\ell d^2)$	$O(\ell d \cdot 2^d)$

#### 4.5 Precontraction Optimization

Since the correction term applies  $A_{\text{trunc}}$  to the Möbius-transformed input  $a = \mu_{\downarrow} v$ , we can precompute the composition:

$$B_{\text{corr}} := A_{\text{trunc}} \circ \mu_{\downarrow}. \quad (14)$$

This allows computing the correction  $C = B_{\text{corr}} \cdot v$  in a single pass. The final FSI is then  $\text{FSI} = \mu_{\downarrow} v + B_{\text{corr}} v$ . Core-level composition sums over the intermediate index  $\tau$ :

$$B_{\text{corr}}^{(k)}[\alpha, \sigma, \rho, \beta] = \sum_{\tau} A^{(k)}[\alpha, \sigma, \tau, \beta] \cdot M[\tau, \rho], \quad (15)$$

where  $M[\tau, \rho] = \delta_{\tau, \rho} - \delta_{\tau, 1} \delta_{\rho, 0}$  is the Möbius matrix. Since  $M$  is  $2 \times 2$ , this simplifies to two cases:  $B^{(k)}[\alpha, \sigma, 0, \beta] = A^{(k)}[\alpha, \sigma, 0, \beta] - A^{(k)}[\alpha, \sigma, 1, \beta]$  and  $B^{(k)}[\alpha, \sigma, 1, \beta] = A^{(k)}[\alpha, \sigma, 1, \beta]$ .

Since  $\mu_{\downarrow}$  has TT-rank 1, precontraction does not increase the bond dimension of  $B_{\text{corr}}$  beyond that of  $A_{\text{trunc}}$  (Lemma 6).

#### 4.6 Complexity Analysis

Table 1 summarizes the complexity of different approaches.

**Time Complexity.** The baseline FSI computation iterates over all  $(S, T)$  pairs where  $T \supseteq S$  and  $|S| \leq \ell$ . The number of such pairs is  $\sum_{t=0}^{\ell} \binom{d}{t} \cdot 2^{d-t}$ , which by the binomial theorem equals  $3^d$  when  $\ell = d$ , but simplifies to  $O(d^\ell \cdot 2^d)$  for fixed  $\ell \ll d$ . SHAP-IQ’s `compute_fii()` follows a similar iteration pattern, plus an  $O(d^{2\ell} \cdot 2^d)$  term from the least-squares solver operating on a  $(2^d \times O(d^\ell))$  matrix.

TT-FSI’s time complexity  $O(\ell^2 d^3 \cdot 2^d)$  has a *fixed polynomial* dependence on  $d$ , independent of  $\ell$ ’s relationship to  $d$ . This yields speedup ratio  $(d^\ell \cdot 2^d) / (\ell^2 d^3 \cdot 2^d) = d^{\ell-3} / \ell^2$ , which grows polynomially for  $\ell \geq 4$  and is  $O(1)$  for  $\ell \leq 3$ . Our experiments at  $\ell \in \{2, 3\}$  show speedups from constant-factor improvements in the TT structure.

**Memory Complexity.** More critically, SHAP-IQ’s `compute_fii()` creates a dense diagonal weight matrix via `np.diag()`, allocating a full  $2^d \times 2^d$  array—hence  $O(4^d)$  memory. This is the root cause of SHAP-IQ’s out-of-memory failures at  $d \geq 16$ . TT-FSI’s core space complexity is **polynomial**  $O(\ell d^2)$ , with peak memory  $O(\ell d \cdot 2^d)$  dominated by the intermediate tensor during contraction. All methods require  $O(2^d)$  space for input  $v$  and output FSI scores.

**NC<sup>2</sup> Complexity.** TT-FSI belongs to NC<sup>2</sup> [4]: the computation can be performed by circuits of depth  $O(\log n \cdot \log \log n)$  where  $n = 2^d$ . This suggests potential for further speedup via GPU parallelization in future work (proof in Appendix C).

## 5 Experiments

We evaluate TT-FSI on six datasets: California Housing [32] ( $d = 8$ ), Diabetes [13] ( $d = 10$ ), COMPAS [2] ( $d = 11$ ), Adult [6] ( $d = 14$ ), Bank Marketing [6] ( $d = 16$ ), and German Credit [6] ( $d = 20$ ), training four model types (DT, XGBoost, LGBM, MLP). We compare against baseline FSI and SHAP-IQ [28] v0.1.1 exact mode; full details in Appendix D.

Table 2: Runtime summary at  $\ell = 3$  (mean over 4 models  $\times$  3 seeds  $\times$  3 runs). Full breakdown in Table 3.

Dataset	$d$	TT-FSI	SHAP-IQ	Baseline	Speedup vs SHAP-IQ	Speedup vs Baseline
California	8	<b>0.8ms</b>	2.5ms	21.7ms	3 $\times$	27 $\times$
Diabetes	10	<b>1.5ms</b>	18.5ms	162.7ms	12 $\times$	105 $\times$
COMPAS	11	<b>2.6ms</b>	89ms	426ms	34 $\times$	164 $\times$
Adult	14	<b>25ms</b>	1997ms	6909ms	80 $\times$	276 $\times$
Bank	16	<b>156ms</b>	OOM*	>1h <sup>†</sup>	—	—
German	20	<b>7.95s</b>	OOM*	>1h <sup>†</sup>	—	—

\*Out of memory. <sup>†</sup>Exceeds time limit ( $O(4^d)$  iterations).

**Accuracy.** TT-FSI produces numerically identical results: max difference vs. baseline is  $8.0 \times 10^{-15}$  (machine precision), vs. SHAP-IQ is  $1.8 \times 10^{-9}$ .

### 5.1 Runtime Performance

Table 2 summarizes runtime performance (full per-model breakdown in Appendix D).

**Speedup Analysis.** TT-FSI outperforms baseline FSI by 20–280 $\times$  across all datasets, with speedup increasing with  $d$ : from  $\sim 27\times$  at  $d = 8$  to  $\sim 276\times$  at  $d = 14$ . This aligns with our complexity analysis—baseline’s  $O(d^\ell \cdot 2^d)$  scaling incurs a polynomial factor that TT-FSI avoids. Beyond  $d = 14$ , baseline becomes impractical due to  $O(4^d)$  nested iterations, while SHAP-IQ exhausts memory ( $O(4^d)$  space). TT-FSI scales gracefully with  $\ell$ , and its efficiency is model-agnostic—runtime depends only on  $d$  and  $\ell$ .

**Comparison with Approximations.** TT-FSI computes *exact* FSI faster than sampling-based approximators. At  $d = 14$ ,  $\ell = 3$ , TT-FSI (41ms) is 8 $\times$  faster than SHAP-IQ Monte Carlo (337ms) and 377 $\times$  faster than SVARM-IQ [24] (15.5s), while approximators incur RMSE of 0.15–0.40 (Table 5 in Appendix).

**Memory and Scaling.** TT-FSI achieves up to **195 $\times$  memory reduction** versus SHAP-IQ at  $d = 14$  (21MB vs 4.1GB), enabling computation at  $d = 20$  where SHAP-IQ requires >60GB. Detailed memory analysis in Appendix D.2.

## 6 Conclusion

We presented TT-FSI, a memory-efficient algorithm for computing Faithful Shapley Interactions via Tensor-Train decomposition. By exploiting the algebraic structure of FSI’s closed form, we achieve TT-rank  $O(\ell d)$  with time complexity  $O(\ell^2 d^3 \cdot 2^d)$  and sparse core storage  $O(\ell d^2)$ . In practice, this translates to up to 280 $\times$  speedup over baseline, 85 $\times$  over SHAP-IQ, and 290 $\times$  memory reduction, enabling successful computation at  $d = 20$  where all existing methods fail due to memory exhaustion.

**Limitations and Future Work.** TT-FSI requires the full  $2^d$  value function, limiting applicability to  $d \lesssim 25$ —sufficient for tabular ML but excluding high-dimensional domains. Future work could combine TT-FSI with sampling-based value estimation, or integrate model-specific optimizations (e.g., TreeSHAP-style algorithms). Our NC<sup>2</sup> result (Appendix C) establishes high parallelizability; GPU experiments (Appendix E) confirm up to 19 $\times$  speedup via Tensor Cores.

## References

[1] Kjersti Aas, Martin Jullum, and Anders Løland. Explaining individual predictions when features are dependent: More accurate approximations to shapley values. *Artificial Intelligence*, 298:103502, 2021.

- [2] Julia Angwin, Jeff Larson, Surya Mattu, and Lauren Kirchner. Machine bias. In *Ethics of data and analytics*, pages 254–264. Auerbach Publications, 2022.
- [3] Marcelo Arenas, Pablo Barceló, Leopoldo Bertossi, and Mikaël Monet. On the complexity of shap-score-based explanations: Tractability via knowledge compilation and non-approximability results. *Journal of Machine Learning Research*, 24(63):1–58, 2023.
- [4] Sanjeev Arora and Boaz Barak. *Computational complexity: a modern approach*. Cambridge University Press, 2009.
- [5] Alejandro Barredo Arrieta, Natalia Díaz-Rodríguez, Javier Del Ser, Adrien Bennetot, Siham Tabik, Alberto Barbado, Salvador García, Sergio Gil-López, Daniel Molina, Richard Benjamins, et al. Explainable artificial intelligence (xai): Concepts, taxonomies, opportunities and challenges toward responsible ai. *Information fusion*, 58:82–115, 2020.
- [6] Arthur Asuncion, David Newman, et al. Uci machine learning repository, 2007.
- [7] Andreas Björklund, Thore Husfeldt, Petteri Kaski, and Mikko Koivisto. Fourier meets möbius: fast subset convolution. In *Proceedings of the thirty-ninth annual ACM symposium on Theory of computing*, pages 67–74, 2007.
- [8] Javier Castro, Daniel Gómez, and Juan Tejada. Polynomial calculation of the shapley value based on sampling. *Computers & operations research*, 36(5):1726–1730, 2009.
- [9] Hugh Chen, Joseph D Janizek, Scott Lundberg, and Su-In Lee. True to the model or true to the data? *arXiv preprint arXiv:2006.16234*, 2020.
- [10] Andrzej Cichocki, Namgil Lee, Ivan Oseledets, Anh-Huy Phan, Qibin Zhao, Danilo P Mandic, et al. Tensor networks for dimensionality reduction and large-scale optimization: Part 1 low-rank tensor decompositions. *Foundations and Trends® in Machine Learning*, 9(4-5):249–429, 2016.
- [11] Ian Covert, Scott Lundberg, and Su-In Lee. Explaining by removing: A unified framework for model explanation. *Journal of Machine Learning Research*, 22(209):1–90, 2021.
- [12] Ian Covert, Scott M Lundberg, and Su-In Lee. Understanding global feature contributions with additive importance measures. *Advances in neural information processing systems*, 33:17212–17223, 2020.
- [13] Bradley Efron, Trevor Hastie, Iain Johnstone, and Robert Tibshirani. Least angle regression. 2004.
- [14] Jerome H Friedman and Bogdan E Popescu. Predictive learning via rule ensembles. 2008.
- [15] Katsuhige Fujimoto, Ivan Kojadinovic, and Jean-Luc Marichal. Axiomatic characterizations of probabilistic and cardinal-probabilistic interaction indices. *Games and Economic Behavior*, 55(1):72–99, 2006.
- [16] Michel Grabisch and Marc Roubens. An axiomatic approach to the concept of interaction among players in cooperative games. *International Journal of game theory*, 28(4):547–565, 1999.
- [17] Riccardo Guidotti, Anna Monreale, Salvatore Ruggieri, Franco Turini, Fosca Giannotti, and Dino Pedreschi. A survey of methods for explaining black box models. *ACM computing surveys (CSUR)*, 51(5):1–42, 2018.
- [18] Peter L Hammer and Ron Holzman. Approximations of pseudo-boolean functions; applications to game theory. *Zeitschrift für Operations Research*, 36(1):3–21, 1992.
- [19] Hiroki Hasegawa and Yukihiko Okada. Interaction tensor shap. *arXiv preprint arXiv:2512.05338*, 2025.
- [20] Giles Hooker. Generalized functional anova diagnostics for high-dimensional functions of dependent variables. *Journal of computational and graphical statistics*, 16(3):709–732, 2007.
- [21] Dominik Janzing, Lenon Minorics, and Patrick Blöbaum. Feature relevance quantification in explainable ai: A causal problem. In *International Conference on artificial intelligence and statistics*, pages 2907–2916. PMLR, 2020.
- [22] Neil Jethani, Mukund Sudarshan, Ian Covert, Su-In Lee, and Rajesh Ranganath. Fastshap: Real-time shapley value estimation. *ICLR 2022*, 2022.

- [23] Tamara G Kolda and Brett W Bader. Tensor decompositions and applications. *SIAM review*, 51(3):455–500, 2009.
- [24] Patrick Kolpaczki, Maximilian Muschalik, Fabian Fumagalli, Barbara Hammer, and Eyke Hüllermeier. Svarm-iq: Efficient approximation of any-order shapley interactions through stratification. *arXiv preprint arXiv:2401.13371*, 2024.
- [25] Scott M Lundberg, Gabriel Erion, Hugh Chen, Alex DeGrave, Jordan M Prutkin, Bala Nair, Ronit Katz, Jonathan Himmelfarb, Nisha Bansal, and Su-In Lee. From local explanations to global understanding with explainable ai for trees. *Nature machine intelligence*, 2(1):56–67, 2020.
- [26] Scott M Lundberg and Su-In Lee. A unified approach to interpreting model predictions. *Advances in neural information processing systems*, 30, 2017.
- [27] Rory Mitchell, Joshua Cooper, Eibe Frank, and Geoffrey Holmes. Sampling permutations for shapley value estimation. *Journal of Machine Learning Research*, 23(43):1–46, 2022.
- [28] Maximilian Muschalik, Hubert Baniecki, Fabian Fumagalli, Patrick Kolpaczki, Barbara Hammer, and Eyke Hüllermeier. shapiq: Shapley interactions for machine learning. *Advances in Neural Information Processing Systems*, 37:130324–130357, 2024.
- [29] Alexander Novikov, Dmitrii Podoprikhin, Anton Osokin, and Dmitry P Vetrov. Tensorizing neural networks. *Advances in neural information processing systems*, 28, 2015.
- [30] Ivan V Oseledets. Tensor-train decomposition. *SIAM Journal on Scientific Computing*, 33(5):2295–2317, 2011.
- [31] Guillermo Owen. Multilinear extensions of games. *Management Science*, 18(5-part-2):64–79, 1972.
- [32] R Kelley Pace and Ronald Barry. Sparse spatial autoregressions. *Statistics & Probability Letters*, 33(3):291–297, 1997.
- [33] Marco Tulio Ribeiro, Sameer Singh, and Carlos Guestrin. “why should i trust you?” explaining the predictions of any classifier. In *Proceedings of the 22nd ACM SIGKDD international conference on knowledge discovery and data mining*, pages 1135–1144, 2016.
- [34] Elina Robeva and Anna Seigal. Duality of graphical models and tensor networks. *Information and Inference: A Journal of the IMA*, 8(2):273–288, 2019.
- [35] Ulrich Schollwöck. The density-matrix renormalization group in the age of matrix product states. *Annals of physics*, 326(1):96–192, 2011.
- [36] Lloyd S Shapley et al. A value for n-person games. 1953.
- [37] Dylan Slack, Sophie Hilgard, Emily Jia, Sameer Singh, and Himabindu Lakkaraju. Fooling lime and shap: Adversarial attacks on post hoc explanation methods. In *Proceedings of the AAAI/ACM Conference on AI, Ethics, and Society*, pages 180–186, 2020.
- [38] Edwin Stoudenmire and David J Schwab. Supervised learning with tensor networks. *Advances in neural information processing systems*, 29, 2016.
- [39] Erik Štrumbelj and Igor Kononenko. Explaining prediction models and individual predictions with feature contributions. *Knowledge and information systems*, 41(3):647–665, 2014.
- [40] Mukund Sundararajan, Kedar Dhamdhere, and Ashish Agarwal. The shapley taylor interaction index. In *International conference on machine learning*, pages 9259–9268. PMLR, 2020.
- [41] Mukund Sundararajan, Ankur Taly, and Qiqi Yan. Axiomatic attribution for deep networks. In *International conference on machine learning*, pages 3319–3328. PMLR, 2017.
- [42] Che-Ping Tsai, Chih-Kuan Yeh, and Pradeep Ravikumar. Faith-shap: The faithful shapley interaction index. *Journal of Machine Learning Research*, 24(94):1–42, 2023.
- [43] Guy Van den Broeck, Anton Lykov, Maximilian Schleich, and Dan Suciu. On the tractability of shap explanations. *Journal of Artificial Intelligence Research*, 74:851–886, 2022.

## A Shapley Interaction Indices

**Shapley Interaction Index (SII).** The SII [16] extends Shapley values via discrete derivatives:

$$\text{SII}_S(v) = \sum_{T \subseteq [d] \setminus S} \frac{|T|!(d - |S| - |T|)!}{(d - |S| + 1)!} \Delta_S v(T), \quad (16)$$

where  $\Delta_S v(T) = \sum_{R \subseteq S} (-1)^{|S| - |R|} v(T \cup R)$ . SII satisfies linearity and symmetry but *not* efficiency for  $|S| > 1$ .

**k-SII.** The k-Shapley Interaction Index [40] aggregates higher-order SII terms to restore efficiency:  $\sum_{|S| \leq \ell} I_S = v([d]) - v(\emptyset)$ .

**Shapley-Taylor Interaction Index (STII).** STII [40] distributes higher-order Möbius coefficients to top-order interactions:

$$\text{STII}_S(v, \ell) = \sum_{T \supseteq S} \frac{(d - |T|)!(|T| - \ell)!}{(d - \ell + 1)!} \Delta_S v(T \setminus S). \quad (17)$$

STII satisfies efficiency but *not* faithfulness.

**Banzhaf Interaction Index (BII).** BII uses uniform weighting instead of Shapley weights, offering computational simplicity.

## B Incidence Algebra Details

The Möbius function on Boolean lattices connects to pseudo-Boolean function approximation [18], where Shapley values and Banzhaf indices arise naturally as best linear approximations. The Möbius function  $\mu$  and zeta function  $\zeta$  on the Boolean lattice [7] are:

$$\mu(S, T) = \begin{cases} (-1)^{|S| - |T|} & T \subseteq S \\ 0 & \text{otherwise} \end{cases}, \quad \zeta(S, T) = \begin{cases} 1 & T \subseteq S \\ 0 & \text{otherwise} \end{cases} \quad (18)$$

These have Kronecker product structure:  $\mu_{\downarrow} = \bigotimes_{i=1}^d M_i$  where  $M_i = \begin{pmatrix} 1 & 0 \\ -1 & 1 \end{pmatrix}$ , implying TT-rank 1.

## C Proofs

**Lemma 2** (Kronecker product has TT-rank 1 [30]). *If a linear operator  $M : \mathbb{R}^{n^d} \rightarrow \mathbb{R}^{n^d}$  has Kronecker product structure  $M = \bigotimes_{i=1}^d M_i$  where each  $M_i \in \mathbb{R}^{n \times n}$ , then  $M$  has TT-rank 1.*

*Proof.* The TT decomposition of  $M$  is given by cores  $G^{(k)} = M_k$  with trivial bond indices (dimension 1). Explicitly, for input index  $\tau = (\tau_1, \dots, \tau_d)$  and output index  $\sigma = (\sigma_1, \dots, \sigma_d)$ :

$$M_{\sigma, \tau} = \prod_{k=1}^d (M_k)_{\sigma_k, \tau_k} = G_{\sigma_1, \tau_1}^{(1)} \cdot G_{\sigma_2, \tau_2}^{(2)} \cdots G_{\sigma_d, \tau_d}^{(d)}. \quad (19)$$

Since all bond dimensions equal 1, the TT-rank is 1. The Möbius operator  $\mu_{\downarrow} = \bigotimes_{i=1}^d \begin{pmatrix} 1 & 0 \\ -1 & 1 \end{pmatrix}$  is a special case.  $\square$

**Lemma 3** (TT-rank upper bound, restated). *The TT-rank of  $A_{\text{trunc}}$  at bond  $k$  is upper bounded by  $O(\ell k)$ .*

*Proof.* Each core slice  $G^{(k)}[\cdot, \sigma, \tau, \cdot]$  is a partial permutation matrix: for each input state  $\alpha_{\text{prev}} = (s_{\text{prev}}, t_{\text{prev}})$ , the output state is uniquely determined by  $(s_{\text{prev}} + \sigma, t_{\text{prev}} + \tau)$  if valid, or the transition is zero. The number of reachable states at position  $k$  is  $|\{(s, t) : 0 \leq s \leq \min(k, \ell), s \leq t \leq k\}| \leq (\min(k, \ell) + 1)(k + 1) = O(\ell k)$ . Since bond indices bijectively encode states, TT-rank equals the number of reachable states.  $\square$

**Lemma 4** (Weight function correctness). *The weight function  $w(s, t)$  in Equation (13) correctly extracts the coefficient from FSI's correction formula (Equation (4)).*

*Proof.* From Equation (4), the correction term for a set  $S$  with  $|S| = s \leq \ell$  is:

$$C_S(v, \ell) = (-1)^{\ell-s} \frac{s}{\ell+s} \binom{\ell}{s} \sum_{\substack{T \supset S \\ |T| > \ell}} \frac{\binom{|T|-1}{\ell}}{\binom{|T|+\ell-1}{\ell+s}} a(v, T). \quad (20)$$

For each superset  $T$  with  $|T| = t > \ell$ , the coefficient of  $a(v, T)$  depends only on  $s = |S|$  and  $t = |T|$ :

$$w(s, t) = (-1)^{\ell-s} \cdot \frac{s}{\ell+s} \cdot \binom{\ell}{s} \cdot \frac{\binom{t-1}{\ell}}{\binom{t+\ell-1}{\ell+s}}. \quad (21)$$

The MPO applies this weight at the final core when the accumulated counters reach  $(s, t)$  with  $s \leq \ell$  and  $t > \ell$ , correctly implementing the correction formula.  $\square$

**Lemma 5** (Time complexity). *The sweep algorithm (Algorithm 1) computes  $M \cdot v$  in  $O(\ell^2 d^3 \cdot 2^d)$  time.*

*Proof.* At step  $k$ , the intermediate tensor has shape  $(2^{k-1}, D_{k-1}, 2^{d-k+1})$  where  $D_k = O(\ell k)$ . The contraction cost is  $O(2^{k-1} \cdot D_{k-1} \cdot D_k \cdot 2^{d-k})$  since each entry involves summing over  $O(1)$  valid transitions. Since  $D_k = O(\ell k)$ , the cost at step  $k$  is  $O(2^d \cdot \ell^2 k^2)$ . Summing over all steps:

$$\sum_{k=1}^d O(2^d \cdot \ell^2 k^2) = O(\ell^2 \cdot 2^d) \sum_{k=1}^d k^2 = O(\ell^2 \cdot 2^d \cdot d^3). \quad (22)$$

$\square$

**Lemma 6** (Precontraction preserves TT-rank). *If  $A$  has TT-rank  $r$  and  $\mu_\downarrow$  has TT-rank 1, then  $B = A \circ \mu_\downarrow$  has TT-rank at most  $r$ .*

*Proof.* The composed core is  $B^{(k)}[\alpha, \sigma, \rho, \beta] = \sum_{\tau} A^{(k)}[\alpha, \sigma, \tau, \beta] \cdot M[\tau, \rho]$ . Since  $M$  is a fixed  $2 \times 2$  matrix (the Möbius matrix), this is a linear combination over  $\tau \in \{0, 1\}$ . The bond indices  $\alpha, \beta$  of  $B^{(k)}$  are identical to those of  $A^{(k)}$ , so the bond dimension is unchanged. Thus  $\text{TT-rank}(B) \leq \text{TT-rank}(A) = r$ .  $\square$

**Lemma 7** (Sparse core storage). *The total storage for MPO cores is  $O(\ell d^2)$ .*

*Proof.* For each state  $\alpha_{\text{prev}} = (s, t)$ , there are at most 3 valid transitions:  $(\sigma, \tau) \in \{(0, 0), (0, 1), (1, 1)\}$  (since  $\tau \geq \sigma$  is required). Thus core  $G^{(k)}$  has at most  $3 \cdot D_{k-1}$  nonzero entries. Since  $D_k = O(\ell k)$ , total storage is:

$$\sum_{k=1}^d O(D_{k-1}) = \sum_{k=1}^d O(\ell k) = O(\ell d^2). \quad (23)$$

$\square$

**Theorem 8** (NC<sup>2</sup> complexity [4], restated). *Let  $n = 2^d$ . FSI computation via TT-FSI can be performed by circuits of depth  $O(\log n \cdot \log \log n)$ .*

*Proof.* The efficient sweep processes  $d = \log n$  sites. Each layer  $k$  computes sums over  $D_k = O(\ell d) = O(\ell \log n)$  bond states. Since  $\ell \leq d$ , we have  $D_k = O(\log^2 n)$ , and each sum uses  $O(\log D_k) = O(\log \log n)$  depth via parallel addition. Total depth:  $O(d \cdot \log \log n) = O(\log n \cdot \log \log n)$ .  $\square$

## D Experimental Details

### Datasets.

- **California Housing** [32] ( $d = 8$ ): Median house values
- **Diabetes** [13] ( $d = 10$ ): Disease progression
- **COMPAS** [2] ( $d = 11$ ): Recidivism risk
- **Adult** [6] ( $d = 14$ ): Income prediction
- **Bank Marketing** [6] ( $d = 16$ ): Term deposit subscription
- **German Credit** [6] ( $d = 20$ ): Credit risk

### Models.

- Decision Tree: `DecisionTreeRegressor(max_depth=6)`
- LightGBM: `LGBMRegressor(n_estimators=30, max_depth=6, n_jobs=-1)`
- XGBoost: `XGBRegressor(n_estimators=30, max_depth=6, device='cuda')`
- MLP: PyTorch, `hidden_sizes=(32,16)`, early stopping

**Value Function.** Interventional:  $v(S) = \mathbb{E}_{X_{\bar{S}}} [f(X_S, X_{\bar{S}})]$ , estimated with 100 background samples. All  $2^d$  coalitions enumerated explicitly (coalition-exact mode).

**Implementation.** Python 3.10, NumPy 1.24, SHAP-IQ v0.1.1. Hardware: Intel Core Ultra 9 (24 cores), 64GB RAM, NVIDIA RTX 5090. Each runtime averaged over 3 seeds  $\times$  3 runs after warm-up.

**TT-FSI Implementation Details.** Our TT-FSI implementation uses single-threaded NumPy operations for the MPO contraction. While NumPy’s BLAS backend may utilize multiple cores for large matrix operations, the sweep algorithm’s sequential structure limits parallelism—each step  $k$  depends on the result of step  $k - 1$ . The  $O(2^d)$  intermediate tensor dominates memory access patterns; at  $d \geq 14$ , this tensor exceeds L3 cache (typically 30–50MB), causing memory-bandwidth-limited behavior. This explains the high variance observed in SHAP-IQ at moderate  $d$  (Table 2): as working sets cross cache boundaries, runtime becomes sensitive to memory access patterns. TT-FSI’s more regular access pattern (sequential sweep) exhibits lower variance. Main experiments use CPU; GPU acceleration results are in Appendix E.

**Runtime Results.** Table 3 provides full runtime breakdown by model. Table 4 provides additional results for  $\ell = 4$ .

At  $\ell = 4$ , TT-FSI achieves up to  $104\times$  speedup over baseline and  $35\times$  over SHAP-IQ Exact. Notably, TT-FSI computes *exact* FSI while being 3–9 $\times$  faster than SHAP-IQ Approx and 197–790 $\times$  faster than SVARM-IQ—both of which are approximate methods with nonzero RMSE.

### D.1 Comparison with Sampling-Based Approximations

TT-FSI computes *exact* FSI while being faster than approximate methods. The approximators incur RMSE of 0.15–0.40 even with budget=10k samples, representing 8–20% relative error on average.

### D.2 Memory Analysis

Figure 2 compares peak memory usage. Baseline is most memory-efficient at  $O(2^d)$  (stores only input/output tensors), but its  $O(4^d)$  time complexity (nested loops over all coalition pairs) makes it impractical for  $d \geq 16$ . SHAP-IQ’s  $O(4^d)$  memory from `np.diag()` causes OOM at  $d \geq 16$ . TT-FSI uses  $O(\ell d \cdot 2^d)$  memory (intermediate tensors during sweep)—more than Baseline but far less than SHAP-IQ. At  $d = 14$ , TT-FSI uses 21MB versus SHAP-IQ’s 4.1GB—a **195 $\times$  reduction**—enabling computation at  $d = 20$  (1.9GB).

Table 3: Full runtime comparison by model (mean $\pm$ std ms, 3 seeds  $\times$  3 runs).

Dataset	Model	$\ell = 2$			$\ell = 3$		
		TT-FSI	SHAP-IQ	Baseline	TT-FSI	SHAP-IQ	Baseline
California ( $d = 8$ )	DT	<b>0.7<math>\pm</math>0.0</b>	1.3 $\pm$ 0.0	14.6 $\pm$ 0.4	<b>0.8<math>\pm</math>0.0</b>	2.4 $\pm$ 0.3	21.9 $\pm$ 0.5
	LGBM	<b>0.7<math>\pm</math>0.0</b>	1.3 $\pm$ 0.0	14.9 $\pm$ 0.2	<b>0.8<math>\pm</math>0.0</b>	2.4 $\pm$ 0.2	21.9 $\pm$ 0.3
	XGB	<b>0.7<math>\pm</math>0.0</b>	1.3 $\pm$ 0.0	14.4 $\pm$ 0.2	<b>0.8<math>\pm</math>0.1</b>	2.5 $\pm$ 0.3	21.2 $\pm$ 0.3
	MLP	<b>0.7<math>\pm</math>0.0</b>	1.3 $\pm$ 0.0	14.6 $\pm$ 0.3	<b>0.8<math>\pm</math>0.0</b>	2.6 $\pm$ 0.4	21.7 $\pm$ 0.5
Diabetes ( $d = 10$ )	DT	<b>1.3<math>\pm</math>0.0</b>	11.6 $\pm$ 1.1	90.6 $\pm$ 1.5	<b>1.6<math>\pm</math>0.0</b>	18.2 $\pm$ 1.3	162.7 $\pm$ 2.1
	LGBM	<b>1.3<math>\pm</math>0.0</b>	11.4 $\pm$ 0.8	90.8 $\pm$ 1.2	<b>1.5<math>\pm</math>0.0</b>	19.3 $\pm$ 2.6	163.0 $\pm$ 2.5
	XGB	<b>1.3<math>\pm</math>0.1</b>	12.5 $\pm$ 1.8	90.9 $\pm$ 1.2	<b>1.5<math>\pm</math>0.0</b>	18.6 $\pm$ 1.3	162.7 $\pm$ 2.6
	MLP	<b>1.3<math>\pm</math>0.0</b>	12.0 $\pm$ 1.5	89.7 $\pm$ 1.5	<b>1.5<math>\pm</math>0.0</b>	18.9 $\pm$ 3.2	162.5 $\pm$ 2.8
COMPAS ( $d = 11$ )	DT	<b>1.9<math>\pm</math>0.0</b>	34.5 $\pm$ 0.8	223.2 $\pm$ 0.4	<b>2.5<math>\pm</math>0.3</b>	68.9 $\pm$ 55	429.7 $\pm$ 0.8
	LGBM	<b>1.9<math>\pm</math>0.0</b>	33.7 $\pm$ 0.4	220.6 $\pm$ 3.1	<b>2.8<math>\pm</math>0.4</b>	95.6 $\pm$ 88	425.2 $\pm$ 6.1
	XGB	<b>1.9<math>\pm</math>0.0</b>	34.1 $\pm$ 0.5	220.9 $\pm$ 3.3	<b>2.6<math>\pm</math>0.4</b>	98.1 $\pm$ 92	425.7 $\pm$ 5.9
	MLP	<b>1.9<math>\pm</math>0.0</b>	34.8 $\pm$ 2.6	220.2 $\pm$ 3.1	<b>2.5<math>\pm</math>0.4</b>	94.2 $\pm$ 83	425.3 $\pm$ 6.5
Adult ( $d = 14$ )	DT	<b>24.5<math>\pm</math>14</b>	1600 $\pm$ 2	3180 $\pm$ 3	<b>24.5<math>\pm</math>2</b>	1988 $\pm$ 8	6901 $\pm$ 7
	LGBM	<b>12.2<math>\pm</math>1</b>	1647 $\pm$ 103	3176 $\pm$ 5	<b>28.6<math>\pm</math>8</b>	2008 $\pm$ 44	6915 $\pm$ 5
	XGB	<b>22.5<math>\pm</math>12</b>	1602 $\pm$ 5	3159 $\pm$ 43	<b>23.6<math>\pm</math>2</b>	1999 $\pm$ 36	6916 $\pm$ 12
	MLP	<b>11.8<math>\pm</math>1</b>	1623 $\pm$ 26	3143 $\pm$ 50	<b>23.6<math>\pm</math>1</b>	1991 $\pm$ 7	6904 $\pm$ 51
Bank ( $d = 16$ )	DT	<b>99<math>\pm</math>13</b>	OOM*	>1h $^\dagger$	<b>156<math>\pm</math>10</b>	OOM*	>1h $^\dagger$
	LGBM	<b>96<math>\pm</math>19</b>	OOM*	>1h $^\dagger$	<b>151<math>\pm</math>11</b>	OOM*	>1h $^\dagger$
	XGB	<b>102<math>\pm</math>35</b>	OOM*	>1h $^\dagger$	<b>155<math>\pm</math>12</b>	OOM*	>1h $^\dagger$
	MLP	<b>106<math>\pm</math>12</b>	OOM*	>1h $^\dagger$	<b>162<math>\pm</math>13</b>	OOM*	>1h $^\dagger$
German ( $d = 20$ )	DT	<b>5944<math>\pm</math>30</b>	OOM*	>1h $^\dagger$	<b>7940<math>\pm</math>61</b>	OOM*	>1h $^\dagger$
	LGBM	<b>5982<math>\pm</math>53</b>	OOM*	>1h $^\dagger$	<b>7946<math>\pm</math>45</b>	OOM*	>1h $^\dagger$
	XGB	<b>5992<math>\pm</math>39</b>	OOM*	>1h $^\dagger$	<b>7992<math>\pm</math>27</b>	OOM*	>1h $^\dagger$
	MLP	<b>5993<math>\pm</math>43</b>	OOM*	>1h $^\dagger$	<b>7947<math>\pm</math>68</b>	OOM*	>1h $^\dagger$

<sup>\*</sup>Out of memory ( $O(4^d)$  space). <sup>†</sup>Exceeds time limit ( $O(4^d)$  iterations).

Table 4: Runtime comparison at  $\ell = 4$  (ms). TT-FSI computes *exact* FSI; approximation methods use budget=10k.

Dataset	$d$	Exact			SHAP-IQ Approx		SVARM-IQ	
		TT-FSI	Baseline	SHAP-IQ	Time	RMSE	Time	RMSE
California	8	<b>0.9<math>\pm</math>0.0</b>	23 $\pm$ 0	4 $\pm$ 1	2.8 $\pm$ 0.1	0.02	177 $\pm$ 3	0.02
Diabetes	10	<b>1.8<math>\pm</math>0.0</b>	219 $\pm$ 1	64 $\pm$ 82	16 $\pm$ 0	0.39	1556 $\pm$ 14	0.39
COMPAS	11	<b>6<math>\pm</math>3</b>	623 $\pm$ 5	211 $\pm$ 221	44 $\pm$ 0	0.03	4745 $\pm$ 27	0.03

### D.3 Bottleneck Analysis

At  $d = 20$ , the total computation time for FSI can be decomposed into two main components:

The key observation is that at large  $d$ , the value function generation (which requires  $2^d$  model predictions) becomes comparable to FSI computation. This suggests two optimization directions: model-specific optimizations where TreeSHAP-style algorithms could compute value functions more efficiently by exploiting tree structure, and approximation schemes using sampling-based approaches that compute a subset of coalitions while maintaining accuracy guarantees.

TT-FSI's efficiency gain is most significant when value functions are precomputed or cheap to evaluate, making the FSI computation itself the bottleneck.

### D.4 Interaction Interpretation

We provide qualitative examples of FSI results on California Housing ( $d = 8$ ) to demonstrate the interpretability of interaction scores.

**Feature Naming.** The 8 features are: MedInc (median income), HouseAge, AveRooms, AveBedrms, Population, AveOccup (average occupancy), Latitude, Longitude.

**Top Pairwise Interactions ( $\ell = 2$ ).** For a randomly selected test instance, the strongest interaction is (Latitude, Longitude) with +0.42, where location features jointly capture geographic value

Table 5: TT-FSI (exact) vs sampling-based approximations (budget=10k).

$d$	$\ell$	TT-FSI	SVARM-IQ	SHAP-IQ <sup>†</sup>	RMSE <sup>‡</sup>
10	2	<b>1.3ms</b>	88ms	6ms	0.21
10	3	<b>1.5ms</b>	449ms	10ms	0.40
12	2	<b>3.2ms</b>	521ms	26ms	0.16
12	3	<b>7.9ms</b>	3,397ms	63ms	0.23
14	2	<b>24ms</b>	2,066ms	178ms	0.15
14	3	<b>41ms</b>	15,473ms	337ms	0.17

<sup>†</sup>SHAP-IQ Monte Carlo mode.

<sup>‡</sup>RMSE of approximators vs TT-FSI ground truth.

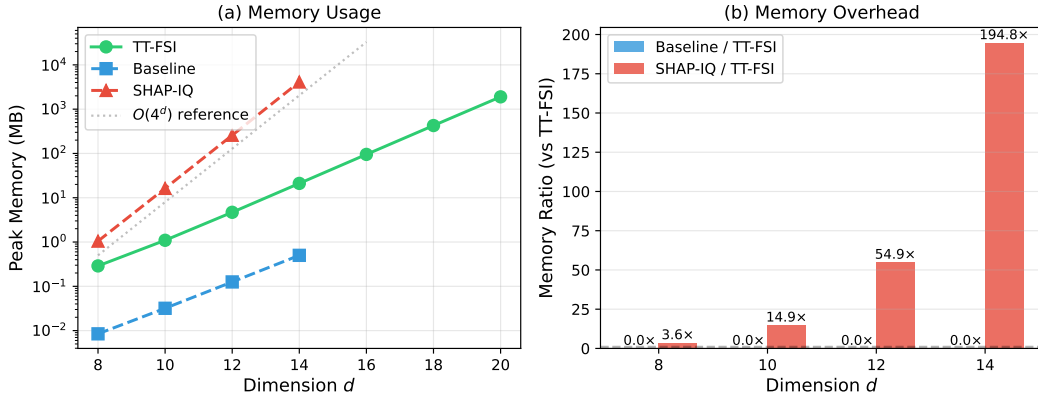


Figure 2: Memory comparison ( $\ell = 3$ ). (a) Peak memory on log scale. Baseline is most memory-efficient but too slow for  $d \geq 16$ . SHAP-IQ exhibits  $O(4^d)$  memory growth. (b) Memory ratio vs TT-FSI.

premium. The pair (MedInc, AveRooms) shows moderate positive interaction (+0.18) as higher income areas with larger homes command premium prices. Conversely, (AveOccup, Population) exhibits negative interaction (−0.15) since these density indicators are partially redundant.

**TT-FSI vs SHAP-IQ Agreement.** Figure 3 shows a scatter plot of all pairwise FSI scores computed by TT-FSI versus SHAP-IQ. The correlation is  $r > 0.9999$ , confirming numerical equivalence. The maximum absolute difference across all  $\binom{8}{2} = 28$  pairs is  $1.2 \times 10^{-10}$ .

## E GPU Acceleration

Our  $NC^2$  complexity result (Theorem in §C) establishes that TT-FSI is highly parallelizable. We validate this by porting TT-FSI to GPU using CuPy and comparing against a vectorized dynamic programming (DP) baseline.

**Implementation.** We port both TT-FSI and a vectorized DP baseline to GPU using CuPy:

- **DP-GPU:** Vectorized dynamic programming with bit-manipulation operations on GPU arrays.
- **TT-GPU:** MPO contraction using `cupy.einsum`. The sweep algorithm maps naturally to GPU tensor operations.

**Results.** Table 8 compares implementations across problem sizes with  $\ell = 3$ .

**Analysis.** The results reveal a clear pattern across problem sizes. For  $d \leq 10$ , DP-CPU is fastest since GPU kernel launch overhead exceeds computational benefits. In the range  $d = 12\text{--}18$ , TT-GPU achieves the best performance with up to  $4.5\times$  speedup over DP-CPU at  $d = 16$ ; the  $NC^2$

Table 6: Peak memory (MB) at  $\ell = 3$ . Baseline:  $O(2^d)$  memory but  $O(4^d)$  time (infeasible at  $d \geq 16$ ).

$d$	TT-FSI	Baseline	SHAP-IQ	Ratio (SHAP-IQ/TT-FSI)
8	0.3	0.01	1.1	$3.6\times$
10	1.1	0.03	16.3	$14.9\times$
12	4.7	0.1	257.6	$54.9\times$
14	21.1	0.5	4105.2	<b>194.8×</b>
16	95.2	SLOW	OOM	—
18	427.0	SLOW	OOM	—
20	1897.3	SLOW	OOM	—

Table 7: Time breakdown at  $d = 20$  (German Credit dataset).

Component	Time (s)	Percentage
Value function generation ( $2^{20}$ predictions)	~2.5	29%
FSI computation ( $\ell = 2$ )	~6.0	71%
FSI computation ( $\ell = 3$ )	~8.0	—

structure of TT-FSI maps efficiently to GPU’s parallel execution model, where `einsum`-based contraction exploits tensor parallelism better than DP’s sequential zeta transforms. For  $d \geq 20$ , DP-GPU becomes faster because TT-rank grows as  $O(\ell d)$ , so the  $D^2$  factor in TT-FSI’s complexity dominates over DP’s  $O(d^2)$  factor at large  $d$ .

**Single-Precision Optimization.** Using `float32` instead of `float64` reveals a striking difference between TT-GPU and DP-GPU. Table 9 shows the impact.

TT-GPU achieves 2–5× speedup with `float32`, while DP-GPU shows no improvement. The reason lies in the computational patterns: TT-GPU’s `einsum`-based contraction is compute-bound, involving tensor contractions where modern GPUs have Tensor Cores optimized for `float32` operations providing 8–16× higher throughput than `float64`. In contrast, DP-GPU’s zeta transform [7] is memory-bound with element-wise additions and array indexing, so the bottleneck is memory bandwidth rather than compute, and `float32` provides no benefit. CPU shows intermediate behavior with TT-FSI gaining 1.5–3.4× from `float32` due to cache efficiency, but lacking Tensor Cores for the dramatic GPU speedup.

**Final Comparison with `float32`.** With single-precision, TT-GPU dominates across all problem sizes:

**Key Findings.** Two factors contribute to TT-FSI’s GPU performance: `float32` with Tensor Cores yields 2–5× speedup from single-precision arithmetic, and the  $NC^2$  structure maps efficiently to GPU Tensor Cores enabling 4–19× speedup over DP-GPU. This validates the practical value of our  $NC^2$  complexity result: TT-FSI’s `einsum`-based contraction is compute-bound and benefits from Tensor Core acceleration, unlike memory-bound DP approaches.

**Precision.** `float32` maintains sufficient accuracy for ML interpretability (relative error < 0.1%).

**Hardware.** GPU experiments conducted on NVIDIA RTX 5090 (32GB) with CuPy 13.6. Times include GPU synchronization to ensure accurate measurement.

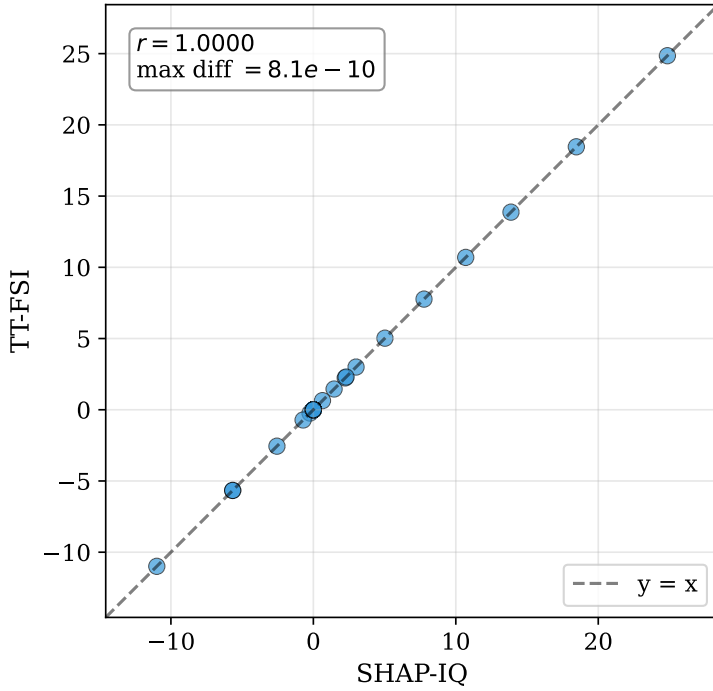


Figure 3: TT-FSI vs SHAP-IQ pairwise interaction scores on California Housing. Perfect agreement (correlation  $> 0.9999$ ).

Table 8: Runtime comparison: CPU vs GPU implementations (ms,  $\ell = 3$ ). Best in **bold**.

$d$	DP-CPU	DP-GPU	TT-GPU	Best Method
12	2.2	24.5	<b>1.4</b>	TT-GPU (1.6 $\times$ )
14	8.4	34.4	<b>2.8</b>	TT-GPU (3.0 $\times$ )
16	37.7	48.2	<b>8.4</b>	TT-GPU (4.5 $\times$ )
18	—	75.0	<b>36.0</b>	TT-GPU (2.1 $\times$ )
20	—	<b>159.1</b>	186.0	DP-GPU (1.2 $\times$ )

Table 9: float32 vs float64 speedup comparison.

$d$	TT-GPU		DP-GPU	
	f64	f32 (speedup)	f64	f32 (speedup)
14	2.8	1.8 (1.6 $\times$ )	34.4	34.5 (1.0 $\times$ )
16	8.4	3.0 (2.8 $\times$ )	48.2	48.1 (1.0 $\times$ )
18	36.0	8.8 (4.1 $\times$ )	75.0	74.5 (1.0 $\times$ )
20	186.0	40.7 (4.6 $\times$ )	159.1	157.7 (1.0 $\times$ )

Table 10: Best methods with float32 optimization (ms,  $\ell = 3$ ).

$d$	TT-GPU (f32)	DP-GPU (f32)	Winner
14	<b>1.8</b>	34.5	TT-GPU (19 $\times$ )
16	<b>3.0</b>	48.1	TT-GPU (16 $\times$ )
18	<b>8.8</b>	74.5	TT-GPU (8 $\times$ )
20	<b>40.7</b>	157.7	TT-GPU (4 $\times$ )